Biosensors and Bioelectronics 26 (2011) 2927–2933

Contents lists available at ScienceDirect

Biosensors and Bioelectronics

journal homepage: www.elsevier.com/locate/bios

Microfluidic chip-based nanoelectrode array as miniaturized biochemical sensing platform for prostate-specific antigen detection

Napat Triroj[a,1], Papot Jaroenapibal[b,2], Haibin Shi[c], Joanne I. Yeh[c,**,3], Roderic Beresford[a,*]

[a] Division of Engineering, Brown University, 182 Hope Street, Providence, RI 02912, USA
[b] Department of Materials Science and Engineering, University of Pennsylvania, 3231 Walnut Street, Philadelphia, PA 19104, USA
[c] Department of Structural Biology and Department of Bioengineering, University of Pittsburgh Medical School, BST3 3501 5th Avenue, Pittsburgh, PA 15213, USA

ARTICLE INFO

Article history:
Received 30 August 2010
Received in revised form
12 November 2010
Accepted 25 November 2010
Available online 3 December 2010

Keywords:
Nanoelectrode arrays
Microfluidic chip
Focused ion beam (FIB)
Prostate-specific antigen (PSA) biosensor
Competitive immunoassay

ABSTRACT

A microfluidic biosensor chip with an embedded three-electrode configuration is developed for the study of the voltammetric response of a nanoelectrode array with controlled inter-electrode distance in a nanoliter-scale sample volume. The on-chip three-electrode cell consists of a 5×5 array of Au working nanoelectrodes with radii between 60 and 120 nm, a Cl_2-plasma-treated Ag/AgCl reference electrode, and a Au counter electrode. The nanoelectrode array is fabricated by creating high-aspect-ratio pores through an alumina insulating layer using an I_2 gas-assisted focused-ion-beam (FIB) milling, ion beam sculpting, and electrodeposition of Au. The glass substrate with the electrode pattern is assembled with a polydimethylsiloxane (PDMS) microchannel slab giving a volume of 180 nL for each channel. Cyclic voltammetry calibration with a standard redox species exhibits a significant increase of current density by two orders of magnitude compared to that obtained from a microelectrode. On-chip functionalization of the nanoelectrodes with a prostate-specific antigen (PSA) biosensor complex and detection of PSA based on a competitive immunoassay method are performed. The detection limit is approximately 10 pg/mL (~270 fM), which corresponds to roughly 30,000 copies of PSA in the microchannel test volume.

1. Introduction

High sensitivity and portability are main requirements for the development of point-of-care testing (POCT) devices. In general, symptoms of diseases or abnormalities are detected at later stages when a large enough number of biomolecules give a significant signal. Device improvements are therefore directed toward miniaturized analytical systems that can provide early detection of diseases which are typically correlated with better prognosis and less invasive treatment plans. For cancer diagnosis, early detection yields higher survival rate because treatment becomes both simpler and more effective. The incorporation of electrochemical sensing modules into a microfluidic chip is recognized as a promising solution for miniaturization of diagnostic devices, to provide simpler manipulation and faster detection of biomolecular processes. A microchannel constitutes self-contained and finely controllable sample handling and delivery to the transducer surface. As biosensors require stable transport of the target molecules to the electrode surface, transducer elements that are accommodated by stable fluidics can operate more effectively. However, one major challenge in developing electrode systems in microfluidic devices is the difficulty to obtain measurable electronic signals and useful information from biomolecular reactions. A nanoliter-scale sample volume of analyte contains only a very small number of molecules that are available to be detected. Thus, robust transducer elements capable of sensing low-level biomolecular signals need to be developed in order to improve sensitivity of the signal response in miniaturized biomedical diagnostic platforms.

The extraordinary properties of nanoscale electrodes for biological measurements have been recognized for some time. For instance, nanoelectrodes provide molecular interfaces to stabilize and access the electroactive centers of redox enzymes, establish effective electrical communication with the probe molecules, and achieve high sensitivity in biomolecular recognition (Shi et al., 2007; Shi and Yeh, 2007; Kovochich et al., 2007; Yeh et al., 2007). These capabilities arise from a critical dimension (e.g. electrode radius) that lies in the range below 100 nm. This length scale is important because it can be comparable to the thickness of the

* Corresponding author. Tel.: +1 401 863 1407; fax: +1 401 863 9107.
** Corresponding author. Tel.: +1 412 648 9027; fax: +1 412 648 9008.
E-mail addresses: napat@elec.kku.ac.th (N. Triroj), papoja@kku.ac.th (P. Jaroenapibal), jiyeh@pitt.edu (J.I. Yeh), rod_beresford@brown.edu, J_Beresford@brown.edu (R. Beresford).
[1] Present address: Department of Electrical Engineering, Khon Kaen University, Khon Kaen 40002, Thailand.
[2] Present address: Department of Industrial Engineering, Khon Kaen University, Khon Kaen 40002, Thailand.
[3] Present address: Department of Structural Biology, University of Pittsburgh School of Medicine, 3501 Fifth Avenue, Pittsburgh PA 15213, USA.

0956-5663/$ – see front matter © 2010 Elsevier B.V. All rights reserved.
doi:10.1016/j.bios.2010.11.039

electrical double layer plus diffuse charge layer, which control the electrochemical reactions. At this scale, the electric field and charge within the near-electrode layers can significantly influence the mass transport and electron transfer kinetics at the electrode surface. Under this electrode configuration, a voltammetric response deviates from classical theory of diffusion-limited current flow (Norton et al., 1990; Smith and White, 1993; He et al., 2006; Yang and Zhang, 2007). For example, the high electric field generated near the electrode surface will cause an enhancement or inhibition of the flux of electroactive species to the electrode surface (Norton et al., 1990). The enhanced electric field is useful for biosensors because high electric field promotes electron tunneling from the electroactive center, which is usually buried within a protein 'shell' of a redox enzyme, to the electrode. Besides these nanoscale effects, enhancement of mass transport may occur and can be understood from classical diffusion models (Wightman and Wipf, 1989). As the electrode size decreases, radial diffusion becomes dominant and the depletion layer thickness approaches the size of the electrode radius (Bard and Faulkner, 1980). Since the rate of mass transport is proportional to the inverse of the depletion layer thickness, a smaller electrode gives a higher measured current density due to a thinner depletion thickness. The high mass transport rate is important when dealing with biomolecular reactions such as catalytic processes, to ensure that the catalytic activity is not controlled by diffusion of the substrate to the electrode (Armstrong, 2005). By employing nanoelectrodes, accurate information from the voltammetric response showing actual enzymatic activity can be obtained when the diffusion of the species to the electrode is enhanced by radial diffusion. Because of these unique response characteristics of nanoscale electrodes, utilizing nanoelectrodes in the construction of electrochemical biosensors will enable significant improvement in electronic transduction.

For nanoelectrode arrays embedded in a microfluidic configuration, the design of a sufficiently large inter-electrode distance (compared to the electrode radius) in order to prevent overlapping of the depletion zones is a method to multiply the current response over that of an individual nanoelectrode. The dynamic behavior of the nanoelectrode array is expected to resemble that of individual nanoelectrodes working in parallel (Morf, 1996; Morf and de Rooij, 1997). Another design consideration is that the insulating layer isolating the underlying wiring layer and separating each individual nanoelectrode in an array should be thick enough to prevent leakage of currents to the underlying conducting layer, and to minimize parasitic capacitive coupling from the planar wiring layer to the solution. In this paper, we develop planar fabrication processes for the construction of well-aligned and low-packing-density nanoelectrode arrays, and for the integration of amperometric electrode cells with microchannel networks to achieve high sensitivity of biomolecular recognition in a nanoliter volume platform. The electrochemical characteristics of the system are investigated with cyclic voltammetry (CV) of a redox process to study the effect of the electrode size on the depletion layer thickness, which influences the current response. In addition, we present results demonstrating the sensitivity of detection that can be achieved for prostate-specific antigen (PSA) utilizing this device.

2. Material and methods

2.1. Chip design, fabrication, and assembly

Fig. 1 shows the layout of the micro-flow chip design, the electrode cell arrangement, and the position of the nanoelectrode array on the working electrode. The configuration of the microelectrode platforms was reported previously (Triroj et al., 2006). In this paper, the working electrode contains 5×5 of 50-nm pore array with

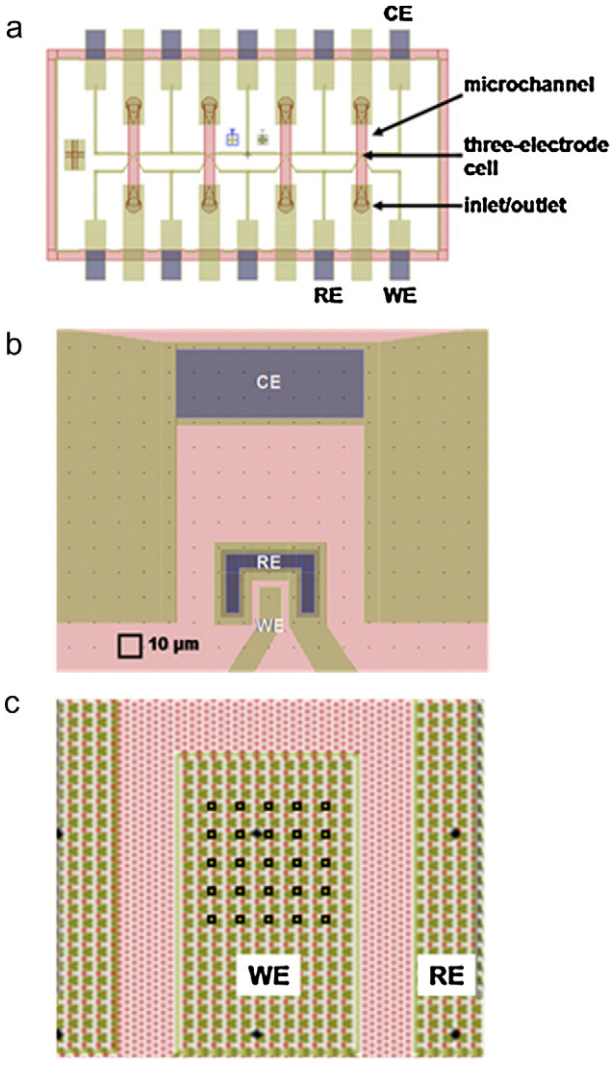

Fig. 1. Design of the electrode pattern and microchannel network. (a) Layout of the chip. (b) Layout of the three-microelectrode cell. (c) Layout of the nanoelectrode array on the working electrode.

the inter-electrode spacing of 1 μm. The inter-electrode distance is sufficiently large compared to the electrode radius to prevent overlapping of depletion zones (Morf, 1996; Morf and de Rooij, 1997).

Microelectrode platforms, interconnecting wires, and probing contact pads composed of 300-nm thick Au and 20-nm Ti as adhesion layer are fabricated on a glass slide using UV lithography, electron-beam evaporation, and lift-off as reported previously (Triroj et al., 2006). For the passivation layer of nanoelectrodes, dense insulating films with the least current leakage are preferred. In this work, electron-beam evaporated alumina is used because it has high density (3.1 g/cm^3) (Gosney and Miller, 1972) and does not require high-temperature processing. The electrode pattern on the glass substrate is processed with UV lithography using 4.5-μm thick AZ® 9245 (Clariant Corporation, Somerville, NJ) photoresist pattern for the subsequent lift-off of alumina films at reference electrodes, counter electrodes, and probing contact pads. Alumina is deposited at the rate of 3 Å/s with the substrate temperature of 200 °C until the resulting film thickness of 720–800 nm is obtained. After the removal of photoresist, the substrate is annealed in air at 300 °C for 4 h in order to reduce the density of interfacial traps and the conductivity of the films, thus increase the packing density of the alumina sheath for better insulating properties.

For the fabrication of the Au nanoelectrode array, we use the FIB (FEI DB235) to mill high-aspect-ratio nanopores through the alumina insulating layer at the working electrode sensing area such that the pores make contact with the underlying metal layer. We employ a gas chemistry to assist in the milling of high-aspect-ratio nanopores. I_2 gas is directed toward the surface of the sample while alumina is being milled with the ion beam. Sputtered material chemically reacts with the assisting gas to form a volatile compound that can be pumped away for faster etching. The Ga^+ ion focused beam current is 10 pA, and ion beam energy is 30 keV. A 5×5 array pattern of 50×50 nm square windows with 1-μm pore-to-pore spacing is defined at each working electrode sensing area. The milling time has been optimized using test samples to obtain the minimum pore openings to expose the buried Au layer, which is needed for the subsequent electrodeposition to create a Au nanoelectrode structure. After milling, the resulting diameters of the nanopores range between 120 and 200 nm. The actual size of the pore window at the surface is typically larger than the targeted milling pattern size and is also dependent on the milling time. To reduce the size of the pore tops to be within the critical dimension for the nanoscale effects to be observed, we use the ion beam sculpting method (Li et al., 2001). Rastering of the ion beam over the whole array using ion beam energy of 30 keV, 10 pA ion beam current, and scanning time of 0.724 s per scan for 15–20 min reduces the initial pore opening diameters to 60–120 nm. Fig. 2a shows a SEM image of a nanopore array after the I_2-gas-assisted FIB milling and ion beam sculpting processes. To obtain a nanoelectrode structure, the pores are then filled by dc electrodeposition of Au at −0.8 V for approximately 2 h in Orotemp 24 gold plating solution ($KAu(CN)_2$ containing 1 troy oz/gallon from Technic Inc., Cranston, RI), using a platinum wire as an anode. Fig. 2b shows a SEM image of the nanoelectrode array on the working electrode after electrodeposition of Au. The image is tilted at 52° with respect to the electron beam showing gold electrodes at the openings of the nanopores. The non-uniformity of Au filling in nanopores is due to the limited capability of FIB instrument to mill the exact same depth and diameter of pores. It can be seen that Au is deposited only inside the nanopore area, indicating that there is no leakage path anywhere else on the alumina surface. Fig. 2c shows a SEM image of the close-up of the tip of an embedded Au nanowire in alumina. The fabrication of Cl_2-plasma treated Ag/AgCl reference electrodes was reported previously (Triroj et al., 2006). After patterning a photoresist layer, electron beam evaporation is used to deposit 20 nm Ti and 1 μm Ag on the reference electrode area. The Ag layer is converted into a Ag/AgCl stack by Cl_2 plasma treatment. The photoresist mask is then removed after plasma chlorination of Ag.

The fabrication process for the PDMS microchannels is similar to what was previously reported (Triroj et al., 2006) with channel depth of 30 μm. After the cleaning process, the complete three-electrode cell array on the glass slide and a PDMS microchannel slab are treated with air plasma, quickly aligned and bonded. An irreversible bond is formed after 24 h of light pressure applied to the bonded substrates. Microtubes are then installed into the inlets and outlets of the microchannels. The PDMS prepolymer is poured over the top of the PDMS microchannel slab to seal the connections. The prepolymer PDMS layer is cured by heating the chip to 65 °C for 30 min. Fig. 2d shows the image of the flow-chip after the bonding process.

2.2. Electrochemical measurement

The instrument for cyclic voltammetry measurements consists of a custom-built potentiostat with a computer-controlled user interface, a Sub-femtoamp Remote SourceMeter (Keithley model 6430), and a shielded probe station. Tungsten tips attached to

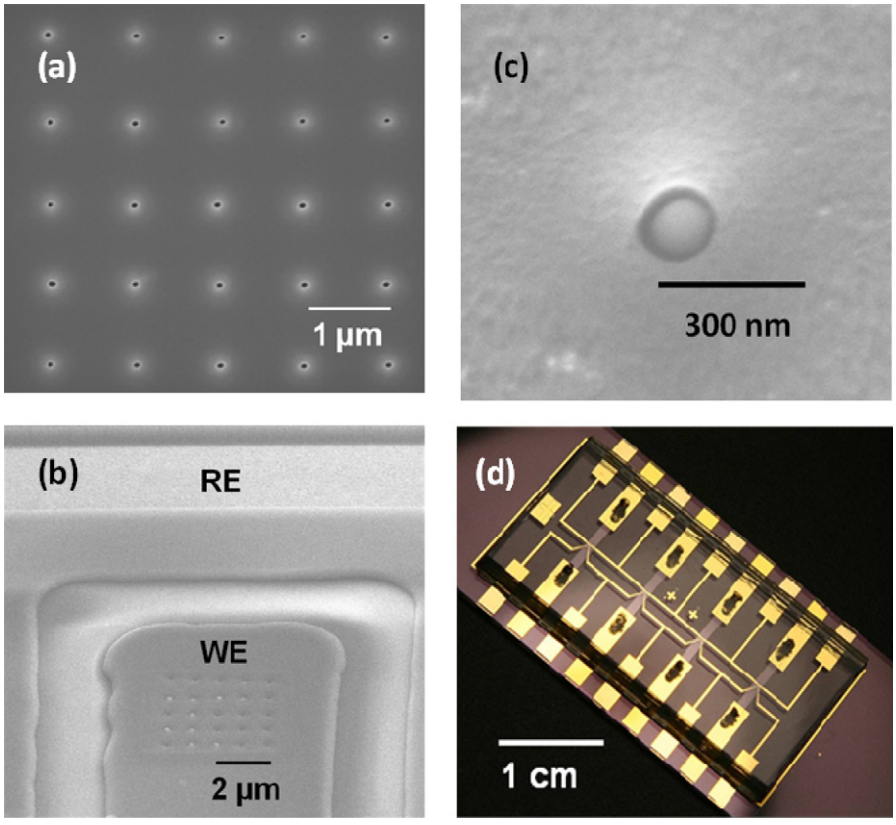

Fig. 2. SEM images showing (a) a nanopore array in alumina insulating layer after the I_2-gas-assisted FIB milling and ion beam sculpting processes, (b) the nanoelectrode array after Au electrodeposition, and (c) a close-up view of a nanoelectrode structure. (d) Final chip after the PDMS microchannel is assembled with the glass substrate.

probe tip holders of the S-725 micropositioners (Signatone, Gilroy, CA) forms good contact with the gold electrode pads on the chip. The LMC662 operational amplifier (National Semiconductor Corp., Santa Clara, CA) is implemented for the potentiostat circuit owing to the low input bias current (2 fA). Keithley 6430 SourceMeter is operated by a LabVIEW program (National Instrument, Austin, TX) and general purpose interface bus (GPIB) communication. A trigger cable is use to synchronize the Keithley 6430 with the National Instrument PCI-6024E data acquisition (DAQ). The DAQ is connected to the potentiostat to output the potential scan and to collect the resulting current response of the system from the data points stored in the buffer layer of Keithley 6430. The recorded data are imported into Excel or MATLAB for analysis.

Calibration of the electrochemical performance of the arrays is carried out by cyclic voltammetry using the analyte solution of 5 mM $Ru(NH_3)_6Cl_3$ in 25 mM sodium phosphate and 25 mM NaCl (pH 7.0). Without further cleaning, a freshly fabricated channel is loaded with the analyte solution using a syringe pump. The syringe pump is turned off after the solution completely fills up the channel. The cyclic voltammograms of the redox reactions from $Ru(NH_3)_6^{3+}/Ru(NH_3)_6^{2+}$ couple are obtained at scan rates of 20, 50, 100, and 200 mV/s. Between each scan, initial conditions at the electrode surface are restored by loading solution into the cell for 1 min at the speed of 2 μL/min, sufficient to replace at least half of the channel volume.

2.3. Functionalized nanoelectrode arrays: PSA biosensor

The functionalization of PSA biosensor system onto the Au electrode surface follows the procedure shown in Fig. 3 (Achim et al., 2009; Yeh et al., 2010a,b). The formation of a self-assembled monolayer is accomplished by adsorption of thiols onto the surface of the Au nanoelectrodes by loading a freshly fabricated channel with 10 mM 3-mercapto-propionic acid (MPA) in ethanol and incubated at room temperature for 1 h. The channel is then flushed with ethanol and DI water. Next, the electrode cell is treated with a solution of 0.2 M N-(3-dimethylaminopropyl)-N′-ethylcarbodiimide (EDC) and 0.05 M N-hydroxysulfosuccinimide (sulfo-NHS) for 1 h at room temperature for activation. After flushing the channel with DI water, the electrode cell is reacted with 115 μg/mL linker complex composed of metalized peptide nucleic acid (M-PNA)–anti-PSA antibody conjugates for 1 h at room temperature to immobilize the linker complex onto the electrode surface. The PNA-anti-PSA antibody assembly was made in co-author J.I. Yeh's group at University of Pittsburgh (Achim et al., 2009; Yeh et al., 2010a,b). The channel is then loaded with 16.5 μg/mL enzyme complex solution which is glucose oxidase (GOx) labelled PSA and incubated overnight at 4 °C to anchor the enzyme complex to the linker component. This electrode assembly is then used as the PSA biosensor. Cyclic voltammetry measurements are carried out from 0 to +700 mV vs. Ag/AgCl reference electrode in 1× phosphate buffered saline (PBS: contains 0.15 M NaCl and 20 mM phosphate saline, $Na_2HPO_4 + NaH_2PO_4$, pH 7.5) with a scan rate of 100 mV/s. For the detection of PSA, the channel is loaded with PSA solutions at different concentrations in 1× PBS buffer and incubated for 5 min prior to the CV measurement. The anodic charge which is the integral of current over time can be obtained from the CV curves using the trapezoidal method. A MATLAB software (function "trapz") is used to compute these data. The anodic charges before and after loading PSA solutions are calculated and plotted versus PSA at different concentrations.

3. Results and discussion

3.1. Voltammetric response of standard redox species

Cyclic voltammograms of the redox process involving $Ru(NH_3)_6^{3+}/Ru(NH_3)_6^{2+}$ in 25 mM Na_2HPO_4 and 25 mM NaCl at different electrode architectures are shown in Fig. 4. $Ru(NH_3)_6^{3+}/Ru(NH_3)_6^{2+}$ as test redox couple were used as these do not adsorb onto the electrode surface (Penner et al., 1990). Fig. 4a shows the CV response at various scan rates of 5 mM $Ru(NH_3)_6Cl_3$ in the electrolyte at a small-radius nanoelectrode array with the estimated surface area of 1.47×10^{-8} cm^2 (see inset), assuming the electrode geometry is hemispherical. With

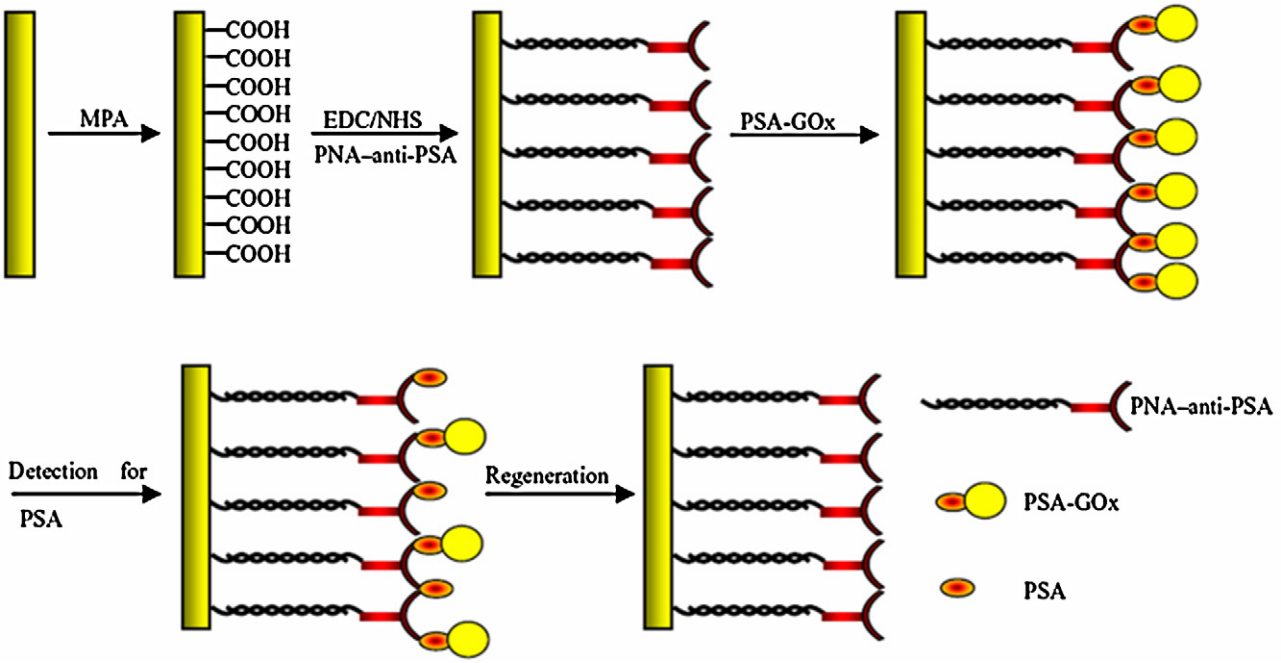

Fig. 3. Schematic diagram of the Au nanoelectrode surface functionalized with GOx and PSA antibody for fabrication of biosensors used in detection of PSA in analyte solutions.

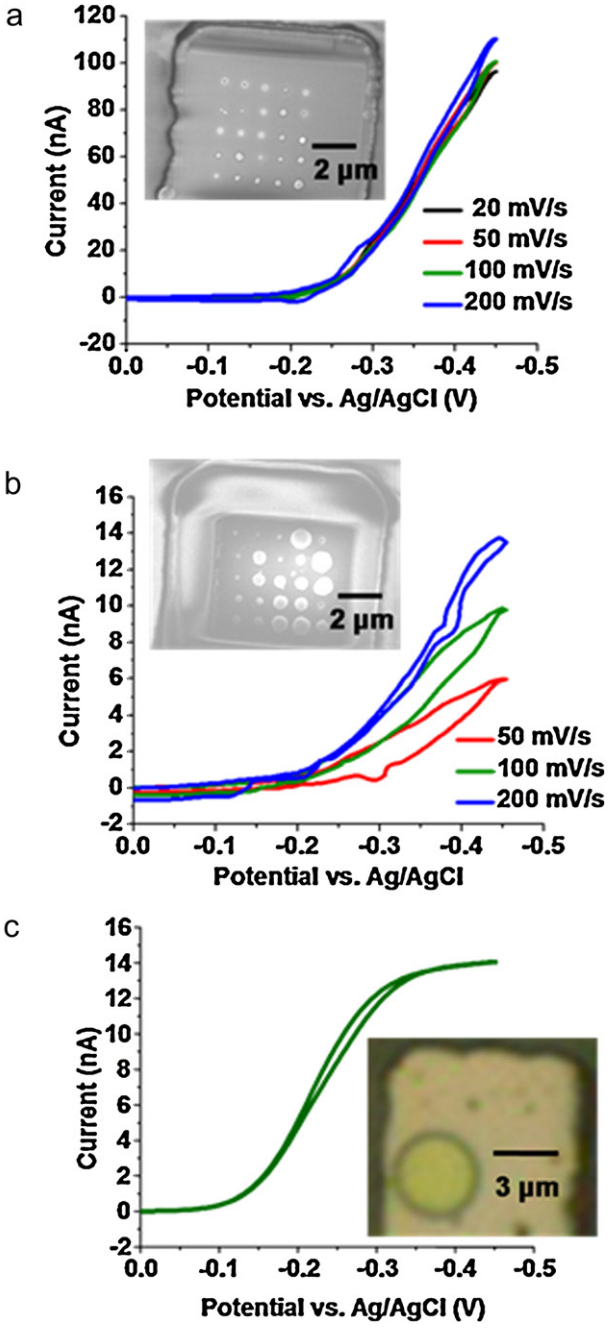

Fig. 4. Cyclic voltammograms of (a) 5 mM $Ru(NH_3)_6Cl_3$ at the small-radius nanoelectrodes. (b) 5 mM $Ru(NH_3)_6Cl_3$ at the large-radius nanoelectrodes. (c) 10 mM $Ru(NH_3)_6Cl_3$ at the microelectrode.

the radius of each electrode close to 100 nm, each nanoelectrode in this case behaves as an individual element because electrode sizes are much less than the gap between them; hence, non-overlapping of the depletion zones can be assumed. At this length scale, the enhancement effect can be quite pronounced. In a dilute solution, there will be a considerable potential drop in the diffuse layer. This high electric field affects the concentration of the electroactive ions at the plane of electron transfer (PET). For the reduction of positively charged ions, an attractive electrostatic force within the diffuse layer accelerates the mass transport of $Ru(NH_3)_6^{3+}$ to the electrode surface. We do not observe a steady-state limiting current plateau in the voltammetric data, as compared to the case of the microelectrode shown in Fig. 4c. This nonclassical behavior

Table 1
Variation in normalized current density (at −0.45 V, 100 mV/s) and $E_{1/2}$ as a function of electrode radius.

Electrode size	Electrode surface area (cm^2)	Normalized current density ($A\,cm\,mol^{-1}$)	$E_{1/2}$ (V)
Small-radius nanoelectrodes (non-overlapped depletion zones)	1.47×10^{-8}	1.36×10^{6}	−0.360
Large-radius nanoelectrodes (overlapped depletion zones)	1.04×10^{-7}	1.92×10^{4}	−0.325
Microelectrode	9×10^{-8}	1.55×10^{4}	−0.230

can be expected from a redox process occurring at nanoelectrodes in a dilute electrolyte (Norton et al., 1990; Chen and Kucernak, 2002). Because of the high mass transport rate due to the coupling between diffusion and migration in the electrode diffuse-layer field, the electron transfer process at the nanoelectrodes is dependent on and controlled by the heterogeneous electrode kinetics (Amatore and Lefrou, 1990). Such an effect is likely the source of the unusual steady-state voltammograms.

Table 1 summarizes the response parameters obtained at different electrode sizes. As the electrode decreases in size, the cathodic wave is shifted to more negative potential. This behavior is ascribed to the enhanced mass transport at the nanoelectrodes (Chen and Aoki, 2002). The normalized current density of the nanoelectrode array in Fig. 4a is calculated to be 1.36×10^6 A cm mol^{-1}, using the estimated surface area from the SEM image. Current density of our nanoelectrode array is increased by two orders of magnitude compared to that (1.55×10^4 A cm mol^{-1}) obtained from the microelectrode in Fig. 4c with the surface area of 9×10^{-8} cm^2, as used in the previous work (Triroj et al., 2006). The current density obtained at the nanoelectrode is also much higher than what is predicted from the theory of steady-state diffusion-controlled current flow for radial diffusion to a hemispherical electrode (Arrigan, 2004). This increase in the current density may result in part from the contributions of migration to mass transport of the reactant. However, it should be emphasized that the surface roughness and different electrode geometry could in fact underestimate the actual electrode surface area, and thus overestimate the true current enhancement factor.

To further investigate the effect of the electrode size on the current response, a large-radius nanoelectrode array is tested with the same concentrations of electroactive species and electrolyte. Fig. 4b shows the CV response of the nanoelectrode array prepared using a longer deposition time of Au. The estimated surface area of the nanoelectrode array is 1.04×10^{-7} cm^2. The dependence of the current response on the scan rates is due to the overlapping of the depletion zones, which causes the mass transport to be governed by linear diffusion. Despite the increase in the surface area compared to that obtained from the nanoelectrodes in Fig. 4a, the magnitude of the current response is significantly lower. The normalized current density at −0.45 V and 100 mV/s of the large-radius nanoelectrodes in Fig. 4b is 1.92×10^4 A cm mol^{-1}. The current density of the nanoelectrode array in Fig. 4b has the same magnitude as that obtained from the microelectrode in Fig. 4c. This result indicates that enhancement of current density is negligible at larger nanoelectrode radius and may be related to the scaling of the electrode dimension into the nanometer regime.

3.2. PSA detection

PSA is a biomarker for prostate carcinoma, and is an established clinical method for diagnosing and monitoring the prostate cancer disease (Chu, 1994). Serum PSA within 4–10 ng/mL is the "diagnostic gray zone," which predicts that the patient has significant probability of prostate carcinoma (Blijenberg et al., 1996). The detection scheme of the PSA biosensor system in this study is based on electrochemical detection, enzyme labels, and a competitive immunoassay method. As shown in Fig. 3, the enzyme (GOx) acts as a redox reporter, stoichiometrically coupling the electrochemical signal to PSA levels in solution. Thus, the magnitude of the current generated as a result of complex formation between the PSA (antigen) and the PSA antibody is directly proportional to the amount of PSA–enzyme conjugates captured by the PSA antibody. When PSA is introduced into the system, PSA will competitively displace the PSA–enzyme conjugates as a consequence of its higher affinity to the anti-PSA antibody compared to the more sterically constrained PSA–enzyme conjugates. The current response decreases due to the elimination of GOx-labelled PSA. Quantitation of the levels of PSA is determined by the magnitude of current decreased, normalized using standard curves generated for each set of biosensors. The preliminary analysis for standard curve generation also is a quality-assurance step as the standard deviations between replicate measurements within and between sample sets are obtained. The 'real-time' performance of these PSA biosensors has been determined by quantitating PSA levels in clinical serum and urine samples (Achim et al., 2009; Yeh et al., 2010a,b), signifying the feasibility of using these biosensors for applications beyond the laboratory setting.

For on-chip PSA detection experiments, we use nanoelectrode arrays of radius smaller than 100 nm to maximize (or increase) sensitivity of the current response and to provide a molecular platform that is less destabilizing to the probed biomolecules. The cyclic voltammograms of the PSA detection performed at scan rate of 100 mV/s in 1× PBS are shown in Fig. 5a. Before loading the PSA solution, rapid and chemically reversible oxidation/reduction of the labelled enzyme is indicated by the symmetric peaks at 0.5 V, shown as the black curve in Fig. 5a. After the PSA solution is loaded into the nanoelectrode array channels, the PSA disrupts the interaction of GOx-PSA and PSA-antibody, and binds PSA-antibody. Displacement of GOx-PSA by PSA is anticipated, due to the higher affinity of PSA to PSA-antibody (7.01×10^{-10} M) compared to the GOx-PSA complex (1.82×10^{-8} M) (Achim et al., 2009; Yeh et al., 2010a,b). The competitive replacement of GOx-PSA by PSA results in concomitant decrease in the amount of the GOx-PSA immobilized on the electrode surface. The resulting decrease in the amount of current generated is directly proportional to amount of PSA conjugates. Therefore, with loading PSA analyte at higher concentrations, the anodic peak current signals decrease, with a shift toward positive potentials. In a situation when PSA biosensor is assumed to be mainly occupied with PSA (PSA concentration of 2 μg/mL in analyte), the cyclic voltammogram (not shown) exhibits disappearance of the anodic peak current due to the elimination of the redox probes (GOx), as expected. The current detection limit for PSA is about 10 pg/mL (~270 fM), which corresponds to roughly 30,000 copies of PSA in the microchannel test volume. Fig. 5b shows the variation of measured anodic charge when different PSA concentrations are added to the system. The experiment is repeated several times, each time with a different nanoelectrode array. The CV curves show a similar trend (i.e. the decrease of anodic currents upon the increment of PSA concentrations in analyte). The data reported here represent the lowest detection limit from our experiment.

To our knowledge, in amperometric detection based on enzyme labels, a detection limit of 4 pg/mL (100 fM) PSA using a single-wall carbon nanotube (SWNT) forest platform has been reported for a few biosensors (Yu et al., 2006). The detection limit of our nanoelectrode array technology is somewhat higher although still competitive. Compared to other approaches, a distinguishing feature of our 'coordinated biosensing' method for sensor fabrication is that the PSA-antibody is precisely linked to a nanoelectrode through a "nano-biolinker" or bridge, the PNA component of the PSA biosensor. The advantage of this PSA biosensor is that the PNA serves as a linker between the molecules and the electrode surface, preventing surface denaturation and directing the electron transfer from the enzyme to the electrode surface which enhances sensitivities of the biosensors. Moreover, another major improvement is that we demonstrate a chip-based platform incorporating a complete electrochemical cell which can detect specific biomolecular signals in nanoliter volumes and in a flow-cell environment. Our reagentless amperometric biosensor system based on electrochemical detection of redox enzyme signals and performance of the biomolecular assembly on a microfluidic platform may be of importance to the development of point-of-care medical diagnostic devices of the future.

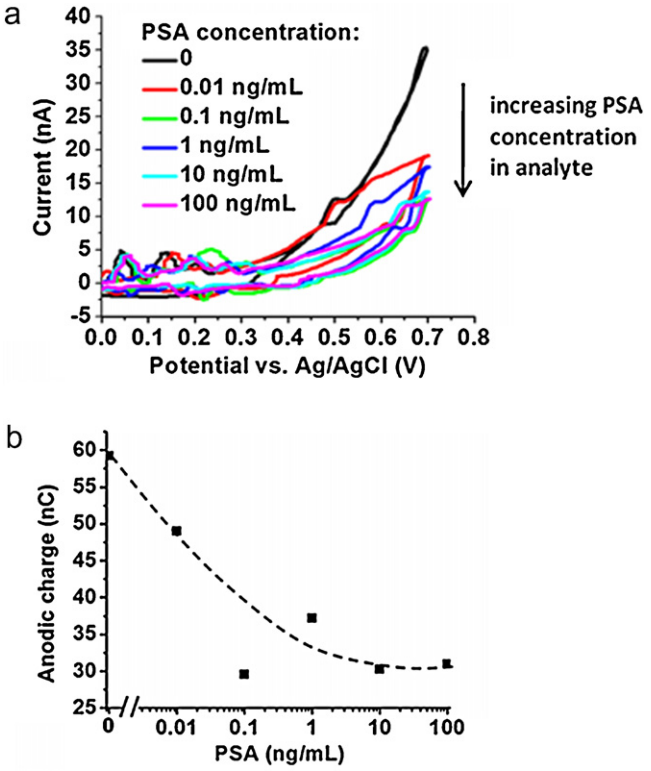

Fig. 5. (a) Cyclic voltammograms of various PSA concentrations in 1× PBS showing the decreasing anodic peak currents as more PSA is added to the system. (b) Measured anodic charge upon addition of PSA.

4. Conclusions

We have fabricated a microfluidic biosensor chip that utilizes well-aligned and low-packing-density nanoelectrode arrays as robust transducer elements for improved sensitivity of the current response in a nanoliter volume testbed. I_2 gas-assisted FIB milling and ion beam sculpting techniques are effective methods to create high-aspect-ratio nanopores with desirable dimensions. The electrochemical calibration of the electrode system with a standard redox species exhibits a significant increase in the current density of the small-radius nanoelectrodes (<100 nm), possibly resulting from electromigration effects within the diffuse layer. The PSA detec-

tion experiment shows that the nanoelectrodes can detect a very small number of PSA molecules in a microfluidic environment. The dynamic range of PSA detection is 0–50 nM. The response time less than 7 s and the detection limit of 270 fM are observed from the sensor. The experimental results demonstrate a promising approach for the development of ultrasensitive bio-signal transducers in a chip-based miniaturized analytical platform. The system is being functionalized with other linker assemblies for the detection of various biomolecular targets with high sensitivity.

Acknowledgment

This work was supported by AFOSR under MURI award F49620-03-1-0365 and, in part, by a grant from National Institutes of Health (GM-66466 to JIY). The authors would like to thank Dr. W.R. Patterson, III and Mr. M. Jibitsky for their assistance with the microfabrication process. The authors also thank Dr. E. Campo of the Penn Regional Nanotechnology facility for her help with the FIB process.

References

Achim, C., Shi, H., Yeh, J.I., 2009, March 5. Biosensors and related methods. United States patent application US 2009/0061451.
Amatore, C., Lefrou, C., 1990. J. Electroanal. Chem. 296, 335–358.
Armstrong, F.A., 2005. Curr. Opin. Chem. Biol. 9, 110–117.
Arrigan, D.W.M., 2004. Analyst 129, 1157–1165.
Bard, A.J., Faulkner, L.R., 1980. Electrochemical Methods: Fundamentals and Application. John Wiley & Sons, New York, NY, p. 208.
Blijenberg, B.G., Kranse, R., Eman, I., Schroder, F.H., 1996. Eur. J. Clin. Chem. Clin. Biochem. 34, 817–821.
Chen, J., Aoki, K., 2002. Electrochem. Commun. 4, 24–29.
Chen, S., Kucernak, A., 2002. J. Phys. Chem. B 106, 9396–9404.
Chu, T.M., 1994. J. Clin. Lab. Anal. 8, 323–326.
Gosney, W.M., Miller, R.S., 1972. Thin Solid Films 14, 255–266.
He, R., Chen, S., Yang, F., Wu, B., 2006. J. Phys. Chem. B 110, 3262–3270.
Kovochich, M., Xia, T., Xu, J., Yeh, J.I., Nel, A.E., 2007. In: M. Weisner, (Ed.), Toxicological Impact of Materials. Principles and Methods for the assessment of nanomaterial toxicity.
Li, J., Stein, D., McMullan, C., Branton, D., Aziz, M.J., Golovchenko, J.A., 2001. Nature 412, 166–169.
Morf, W.E., 1996. Anal. Chim. Acta 330, 139–149.
Morf, W.E., de Rooij, N.F., 1997. Sens. Actuator B 44, 538–541.
Norton, J.D., White, H.S., Feldberg, S.W., 1990. J. Phys. Chem. 94, 6772–6780.
Penner, R.M., Heben, M.J., Longin, T.L., Lewis, N.S., 1990. Science 250, 1118–1121.
Shi, H., Yeh, J.I., 2007. Nanomedicine 2 (5), 587–598.
Shi, H., Xia, T., Nel, A.E., Yeh, J.I., 2007. Nanomedicine 2 (5), 599–614.
Smith, C.P., White, H.S., 1993. Anal. Chem. 65, 3343–3353.
Triroj, N., Lapierre-Devlin, M.A., Kelley, S.O., Beresford, R., 2006. IEEE Sens. J. 6, 1395–1402.
Wightman, R.M., Wipf, D.O., 1989. In: Bard, A.J. (Ed.), Electroanalytical Chemistry, vol. 15. Marcel Dekker, New York, p. 267.
Yang, X., Zhang, G., 2007. Nanotechnology 18, 335201.
Yeh, J.I., Du, S., Xia, T., Lazareck, A., Kim, J.-H., Xu, J., Nel, A.E., 2007. ECS Transactions 3 (29), 115–126.
Yeh, J.I., Shivachev, B., Rapireddy, S., Gil, R.R., Du, S., Ly, D., 2010a. J. Am. Chem. Soc. 132 (31), 10717–10727.
Yeh, J.I., Pohl, E., Truan, D., He, W., Sheldrick, G., Du, S., Achim, C., 2010b. Chem. Eur. Journal 16 (39), 11867–11875.
Yu, X., Munge, B., Patel, V., Jensen, G., Bhirde, A., Gong, J.D., Kim, S.N., Gillespie, J., Gutkind, J.S., Papadimitrakopoulos, F., Rusling, J.F., 2006. J. Am. Chem. Soc. 128, 11199–11205.